Journal of Pharmaceutical Analysis 15 (2025) 101085

Contents lists available at ScienceDirect

Journal of Pharmaceutical Analysis

journal homepage: www.elsevier.com/locate/jpa

Original article

Coupling of an Au@AgPt nanozyme array with an micrococcal nuclease-specific responsiveness strategy for colorimetric/SERS sensing of *Staphylococcus aureus* in patients with sepsis

Xueqin Huang [a, b, 1], Yingqi Yang [a, 1], Hanlin Zhou [a], Liping Hu [a], Annan Yang [a], Hua Jin [b], Biying Zheng [b], Jiang Pi [b], Jun Xu [a], Pinghua Sun [a, c], Huai-Hong Cai [d], Xujing Liang [e, ****], Bin Pan [e, ***], Junxia Zheng [f, **], Haibo Zhou [a, *]

[a] College of Pharmacy, The Second Clinical Medical College (Shenzhen People's Hospital), The Fifth Affiliated Hospital, Jinan University, Guangzhou, 510632, China
[b] Research Center of Nano Technology and Application Engineering, The First Dongguan Affiliated Hospital, School of Medical Technology, Guangdong Medical University, Dongguan, Guangdong, 523000, China
[c] School of Pharmacy, Shihezi University, Shihezi, Xinjiang, 832003, China
[d] College of Chemistry and Materials Science, Jinan University, Guangzhou, 510632, China
[e] The First Affiliated Hospital of Jinan University, Jinan University, Guangzhou, 510632, China
[f] School of Biomedical and Pharmaceutical Sciences, Guangdong University of Technology, Guangzhou, 510006, China

ARTICLE INFO

Article history:
Received 1 May 2024
Received in revised form
18 August 2024
Accepted 22 August 2024
Available online 27 August 2024

Keywords:
Au@AgPt nanoarrays
Surface-enhanced Raman scattering
Colorimetry
Cascade response strategy
MNase

ABSTRACT

Rapid and ultrasensitive detection of pathogen-associated biomarkers is vital for the early diagnosis and therapy of bacterial infections. Herein, we developed a close-packed and ordered Au@AgPt array coupled with a cascade triggering strategy for surface-enhanced Raman scattering (SERS) and colorimetric identification of the *Staphylococcus aureus* biomarker micrococcal nuclease (MNase) in serum samples. The trimetallic Au@AgPt nanozymes can catalyze the oxidation of 3,3',5,5'-tetramethylbenzidine (TMB) molecules to SERS-enhanced oxidized TMB (oxTMB), accompanied by the color change from colorless to blue. In the presence of *S. aureus*, the secreted MNase preferentially cut the nucleobase AT-rich regions of DNA sequences on magnetic beads (MBs) to release alkaline phosphatase (ALP), which subsequently mediated the oxTMB reduction for inducing the colorimetric/SERS signal fade away. Using this "on-to-off" triggering strategy, the target *S. aureus* can be recorded in a wide linear range with a limit of detection of 38 CFU/mL in the colorimetric mode and 6 CFU/mL in the SERS mode. Meanwhile, the MNase-mediated strategy characterized by high specificity and sensitivity successfully discriminated between patients with sepsis ($n = 7$) and healthy participants ($n = 3$), as well as monitored the prognostic progression of the disease ($n = 2$). Overall, benefiting from highly active and dense "hot spot" substrate, MNase-mediated cascade response strategy, and colorimetric/SERS dual-signal output, this methodology will offer a promising avenue for the early diagnosis of *S. aureus* infection.

1. Introduction

Staphylococcus aureus is the leading cause of hospital- and community-acquired infections [1]. The presence of *S. aureus* in the blood can lead to severe sepsis, a systemic inflammatory response characterized by fever, infection, and poisoning symptoms. Sepsis caused by *S. aureus* combines inflammation and immunosuppression, and renders the host defenseless against disease-causing pathogens and secondary infections, leading to fatal organ dysfunction [2]. Therefore, point-of-care (POC) and unltrasensitive recognition of *S. aureus* in clinical samples (e.g., saliva and blood) would be conducive to early intervention and drug choices for treating bacterial infections. Currently, analysis based on species-specific biomarker has been applied as an ideal alternative for microbiological analysis given their convenience, simplicity and practicability. Micrococcal nuclease (MNase) is a unique exoenzyme excreted by *S. aureus* that preferentially digests single-

* Corresponding author.
** Corresponding author.
*** Corresponding author.
**** Corresponding author.
E-mail addresses: xjlxj.lxj@163.com (X. Liang), panbin@jnu.edu.cn (B. Pan), junxiazheng@gdut.edu.cn (J. Zheng), haibo.zhou@jnu.edu.cn (H. Zhou).
Peer review under responsibility of Xi'an Jiaotong University.
[1] Both authors contributed equally to this work.

https://doi.org/10.1016/j.jpha.2024.101085

stranded DNA and double-stranded DNA and RNA, especially those in the AT- or AU-rich regions [3]. Furthermore, this MNase remains stable and active even after incubation at 97 °C for 1 h [4]. More importantly, there is a remarkable correlation between thermostable MNase and *S. aureus* count [5], making it a reliable indicator for diagnosing diseases caused by *S. aureus*. Several techniques have been proposed for detecting MNase, including enzyme linked immunosorbent assay (ELISA), polymerase chain reaction (PCR), and gel electrophoresis; however, these methods require complicated sample pretreatment, long procedural times (approximately days) and professional technical users, which, in turn, obsolete their widespread application [6,7]. Despite molecular imaging, various methods such as fluorescence and colorimetric assay with merit of convenient and fast response are promising for detection of MNase; however, these methods are relatively less sensitive and prone to interference [8–10]. Therefore, developing a highly sensitive, simple and fast strategy for MNase analysis remains supremely important.

Surface-enhanced Raman scattering (SERS) has emerged as a fascinating analytical method for the rapid, highly sensitive and specific detection of various biomarkers [11–13]. Owing to localized surface plasmon resonance (LSPR), the electromagnetic field enhancement ("hot spots") formed by the rough surfaces, tips or nanogaps of plasma substrates vigorously causes SERS effect, from which single molecule detection can be realized [14–16]. Particularly, by integrating different functional properties of metals, multimetallic nanoparticles (NPs) open the possibility for marrying plasmonic and catalytic properties, which is defined as a nanozyme [17–20]. Such nanozyme can directly catalyze the conversion of certain organic dyes into SERS-active molecules, accompanied with alteration of colorimetric/SERS signal [21–23], thus offering significant potential in catalysis-based SERS assays. More importantly, SERS technology can monitor changes in substances adsorbed on catalyst surfaces and detect enzyme-like reaction kinetics occurring on the interface or surface of nanozyme [24,25]. Our previous study proposed Au@AgPt nanozyme for *in situ* SERS monitoring of plasmon-mediated halogenated benzene dehalogenated coupling reaction [17]. Regrettably, weak SERS signals attributed to the coverage of Pt shell that shielded the plasmonic performance would somewhat limit the ultratrace detection. Although the aforementioned issue could be effectively tackled by controlling the thickness of the Pt shell on the surface of plasmonic NPs [26,27], the poor reproducibility caused by the stochastic aggregation of the colloidal system in the sample solution remained quite challenging for SERS-based detection.

One fascinating strategy for enhancing the consistency of SERS analysis is to construct a well-ordered nanostructured array. In such arrays, the coupling effect between adjacent repeating units creates a dense plasmonic network on the film surface, enabling strong and uniform enhancement of the electromagnetic effect in terms of intensity and spatial distribution [28,29]. Additionally, an open and wide surface can easily capture and absorb more targets into the regions of "hot spots" for SERS signal high and stable output. Until now, a variety of techniques for preparing SERS-active plasmonic nanoarray have been reported, among which the bottom-up self-assembly of nanomaterials on the immiscible water-oil interface stands out as one of the most favorable tools on account of its simple preparation, high reproducibility, low-cost engineering and defect-free characteristics. As a result, several types of homogenous plasmonic array substrates have been successfully proposed with regular patterns, such as gold nanospheres, gold nanorods, and gold trisoctahedron arrays [30–33]. However, despite the gold nanostructures with uniform distribution were beneficial for forming highly ordered arrays, few studies focused on developing self-assembled multimetallic NP arrays for achieving nanozyme catalyzed-SERS sensing.

In this work, a novel Au@AgPt trimetallic nanozyme was self-assembled into a close-packed array with an ordered distribution of "hot spots" via a bottom-up approach (Scheme 1A). Herein, the Au@AgPt nanozyme catalyzes the conversion of colorless 3,3',5,5'-tetramethylbenzidine (TMB) molecules into blue-colored oxidized TMB (oxTMB) with strong Raman response through the deposited Pt shell, and concomitantly the Au/Ag core acts as a SERS substrate to amplify the SERS-active oxTMB signal. Thus, a simple and sensitive Au@AgPt array-mediated sensing platform was developed for colorimetric/SERS dual-mode identifying *S. aureus* indicator MNase. As presented in Scheme 1B, the heat-treated MNase can cleave the AT-rich regions of alkaline phosphatase-oligonucleotide-connected magnetic beads (ALP-DNA-MBs), releasing ALP. After magnetic separation, the free ALP catalyzed conversion of L-ascorbic acid 2-phosphotrisodium salt (AAP) into ascorbic acid (AA), which subsequently mediated the reduction of oxTMB to nonresponsive TMB, resulting in the colorimetric and SERS signal fade away on the Au@AgPt array (Scheme 1C). In this case, the colorimetric and SERS signal of the composite system exhibits a negative correlation with the concentration of MNase, allowing it suitable for quantitative analysis of MNase excreted from *S. aureus* in real infected samples. This Au@AgPt array sensing system possessed the following three prominent properties: 1) the close-packed arrays has a large surface area that allows the molecules to be effectively confined to the nanogap, where the high density and uniform "hot spots" enable strong and highly reproducible output of the signal; 2) trimetallic Au@AgPt incorporated plasmonic and nanozyme-catalytic activities for colorimetric/SERS sensing, which inherited the advantage of each mode and provided double insurance on the same analysis to drastically reduce false positive or false results; 3) crucially, the "on-to-off" ingenious strategy that initiated through the cascade triggering procedure was favorable for improving anti-interference and specificity in MNase measurement. Thus, by integrating the merits of well-distributed array, MNase-specific responsiveness, and colorimetric/SERS dual-mode sensing, the proposed platform held a great potential for diagnosing and predicting the prognosis of infectious diseases caused by *S. aureus*.

2. Experimental

2.1. Materials and reagents

Hydrogen tetrachloroaurate ($HAuCl_4 \cdot 3H_2O$), silver nitrate ($AgNO_3$), AA, trisodium citrate, chloroplatinic acid hexahydrate ($H_2PtCl_6 \cdot 6H_2O$), TMB, and phosphate-buffered saline (PBS) were supplied by Macklin (Shanghai, China). Exonuclease (Exo III and Exo I), deoxyribonuclease I (DNase I), MNase, and biotin-DNA oligonucleotide (biotin-DNA) were obtained from Sangon Biotech Co. Ltd. (Shanghai, China). The biotin-DNA oligonucleotide sequences were 5'-biotin-AAAAAAAAAAAATATATAGATAGCATCGGACA-3', and their partially complementary sequences were 5'-biotin-AAAAAAAAAAAATGTCCGATGCT-3'. AAP, streptavidin (SA)-ALP, and SA functionalized magnetic beads (SA-MBs) were obtained from Sigma Co., Ltd. (St. Louis, MO, USA). The water used in this study was purified via an ultrafilter system (Milli-Q, Millipore, Marlborough, MA, USA). The blood samples were kindly provided by the Second Affiliated Hospital of Jinan University (Shenzhen, China).

2.2. Synthesis of Au@AgPt NPs

The fabrication process of Au@AgPt NPs is schematically illustrated in Scheme 1A. In brief, the Au NPs as the seeds were first synthesized by a previously reported method [34,35]. Then, the fabricated Au seed solution (1 mL) was diluted with an aqueous solution (11.5 mL) containing 1.8 mL of cetyltrimethylammoniumchloride (CTAC, 10 mM)

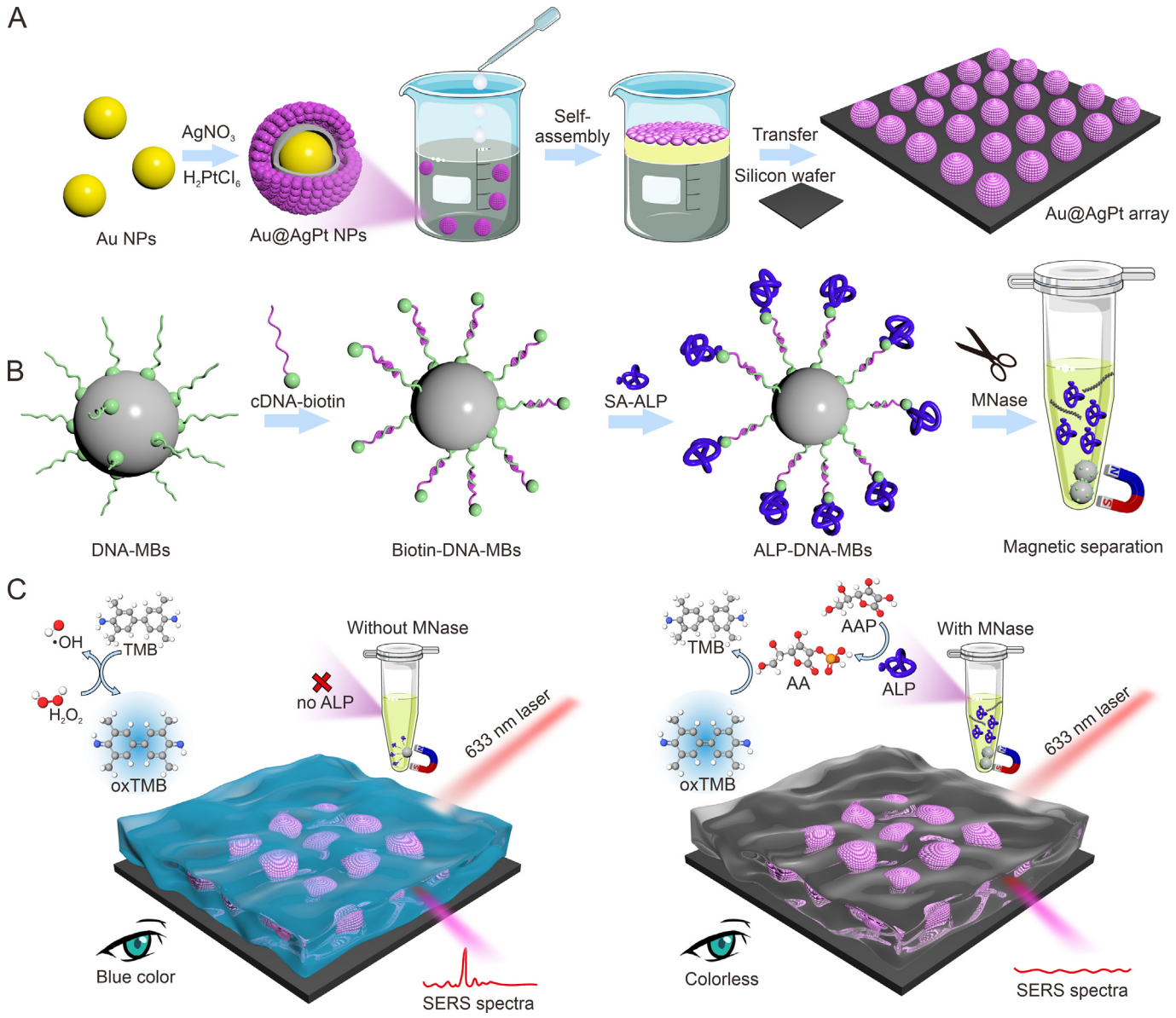

Scheme 1. Colorimetric/surface-enhanced Raman scattering (SERS) sensing for micrococcal nuclease (MNase)-responsive detection. (A) Interfacial self-assembly process for Au@AgPt array. (B) Preparation process of alkaline phosphatase (ALP)-DNA-magnetic beads (MBs) through the interplay between biotin-DNA-MBs and streptavidin (SA)-ALP. (C) Principle of Au@AgPt array-mediated cascade triggering strategy for colorimetric/SERS dual-mode detection of MNase. NPs: nanopatricles; cDNA: complementary DNA; TMB: 3,3',5,5'-tetramethylbenzidine; oxTMB: oxidized TMB; AA: ascorbic acid; AAP: L-ascorbic acid 2-phosphotrisodium salt.

with stirring under 25 °C. After 10 min, 100 μL of AA (100 mM) and 50 μL NaOH (200 mM) were added into the mixture and stirred vigorously for another 30 min. Subsequently, 1 mL of $AgNO_3$ (10 mM) was added rapidly, with the change of color from wine-red to saffron yellow. 0.5 mL of H_2PtCl_6 (10 mM) was then injected (one drop per 40 s) under vigorous shaking. After H_2PtCl_6 drops addition completely, the solution continued to react for 30 min to form Au@AgPt NPs with dark brown color. The products were collected by centrifugation (10,000 rpm, 5 min) and washed thrice with deionized water, then stored at 4 °C for future use. In this experiment, Au@AgPt NPs with various of shell thicknesses were fabricated by controlling the volume ratio of $AgNO_3$ and H_2PtCl_6 (5:1, 3:1, 2:1, 1:1, 1:2, 1:3, and 1:5, *v/v*) while keeping the total volume constant.

2.3. Self-assembly of Au@AgPt NPs for preparing an array

We assembled the Au@AgPt array at the water-hexane interfacial system. The Au@AgPt NPs colloid (6 mL) was poured into the clean glass beaker, and hexane (2 mL) was added slowly to form an immiscible liquid system. After that, ethanol (1.5 mL) as the inducer was then added into the mixed solution to entrap Au@AgPt NPs at the water-hexane interface by decreasing the interfacial energy. The entrapped Au@AgPt NPs were self-assembled into a monolayer film with the evaporation of organic phase solution spontaneously. Finally, the above-mentioned Au@AgPt array was transferred and fixed onto a clean silicon wafer using a method described previously [36] and air-dried at room temperature.

2.4. Preparation of ALP-DNA-modified MBs

ALP-DNA-modified MBs were constructed based on the principle of complementary pairing. In detail, 100 μL of SA-MBs (4 mg/mL) were washed three times with sterile deionized water and re-dispersed in 100 μL of 1% bovine serum albumin (BSA) solution. Subsequently, 4 μL of biotin-DNA oligonucleotide (100 μM) was added, incubated at 25 °C for 60 min with continuous shaking, and washed three times to remove excess unbound biotin-DNA. Then, the DNA-functionalized MBs were obtained through the interaction between biotin and SA, and they were re-suspended in 100 μL of a binding buffer solution for reaction with 4 μL of biotin-complementary DNA (cDNA) oligonucleotide (100 μM). After incubation at 25 °C for 1 h, the resulting biotin-DNA-MBs were collected using a magnetic force and washed three times to remove the unreacted biotin-cDNA. Finally, biotin-DNA-MBs were mixed with 4 μL of SA-ALP (1 mg/mL) in binding buffer and gently stirred for 1 h. The prepared ALP-DNA-MBs were separated, washed, dispersed as described above, and stored at 4 °C for further use.

2.5. Characterization

The ultraviolet−visible (UV−vis) absorption spectra were obtained by UV−vis-NIR spectrophotometer (Shimadzu UV-3600, Shimadzu Co., Tokyo, Japan). The ζ potential and morphology were measured using the Malvern Nanoparticle size & zeta potential analyzer (Nano ZS, Malvern Panalytical, Worcestershire, UK) and field-emission transmission electron microscopy (TEM) analysis (JEM-2100F, JEOL Ltd., Tokyo, Japan), respectively. The morphology of the Au@AgPt array was observed using a scanning electron microscopy (SEM) equipment (Merlin, Zeiss, Oberkochen, Germany) and an atomic force microscopy (AFM) system (Bioscope Catalyst, Bruker, Bremen, Germany), which provided the topographical and corresponding three-dimensional (3D) images. Element composition was assessed using energy-dispersive X-ray (EDX) and X-ray photoelectron spectroscopy (XPS) analysis (PHI 5000 Versa Probe, ULVAC-PHI, Tokyo, Japan). SERS spectra were measured by a Raman microscope (LabRAM HR, Horiba Ltd., Kyoto, Japan) equipped with a 633-nm extinction laser (2s of accumulation) and 50× objective lens (NA = 0.75), optimized for maximum Raman intensity. Data acquisition and processing were performed using the LabSpec software, and all Raman spectra were presented after baseline adjustment.

2.6. Detection of MNase activity

MNase enzymes were incubated at 95 °C for 10 min before use due to their thermoresistance property, while other interfering enzymes or proteins were denatured to exclude interference. For MNase assays, ALP-DNA-MBs (15 μL) were mixed MNase with different concentrations, and placed at 37 °C for 30 min. After convenient magnetic separation, supernatants (25 μL) was collected and mixed with Tris-HCl buffer (200 μL, pH 9.0) and 25 μL of AAP solution (10 mM) evenly, followed by pre-reaction for 30 min. Then, acetate buffer (160 μL, 50 mM, pH 4.0), colorless TMB (20 μL, 3 mM) and H_2O_2 (20 μL, 600 mM) were added to the self-assembled Au@AgPt array silicon wafers, and reacted for 30 min to form stable blue oxTMB. Finally, the 50 μL of resulting solutions were mixed to the oxTMB solution on the silicon wafer, the optical images were then recorded, and SERS spectra of TMB oxidation were determined immediately. For UV−vis analysis, the oxTMB solutions were transferred to the microplate to obtain the absorption spectra.

To detect the MNase released from *S. aureus*, we centrifugated a series of bacterial standard suspensions with concentrations of 10^1–10^8 CFU/mL. The supernatant was collected, boiled, incubated and treated as described above. In view of the high ionic strength and salt concentration in the serum which may affect analysis stability [37], the patient serum was diluted to 1% with PBS for all subsequent experiments.

2.7. Evaluation of selectivity and anti-interference of assay

To evaluate the anti-interference of the assay, we also measured several other nucleases, namely Exo III, Exo I, and DNase I (800 U/L), under the same experimental conditions as those for MNase detection. To assess the selectivity of the assay, we tested different types of bacteria (*Escherichia coli* and *Pseudomonas aeruginosa*) and bacterial mixtures. To determine the stability and repeatability, we stored the Au@AgPt array in the dark at 4 °C for varying durations before conducting MNase detection using SERS and colorimetric sensing. To increase statistical reliability, we collected data from at least 10 different points within each group and averaged the values as the final result. The limit of detection (LOD) was calculated based on the ratio of the standard deviation (SD) of the blank to the slope of the linear equation of the calibration plot (LOD = 3SD/slope, n = 3).

2.8. Statistical analysis

We conducted all experiments at least thrice and all data presented as mean ± standard deviation (SD). Statistical significance was assessed using analysis of variance, supplemented by independent *t*-tests for pairwise comparisons. P values of < 0.05 were considered as statistically significant.

3. Results and discussion

3.1. Synthesis and characterization of Au@AgPt NPs

In this study, by incorporating the advantages of the well-known plasmonic activities of Au/Ag and peroxidase-like properties of Pt, the trimetallic Au@AgPt NPs perform superior plasmonic and catalytic activity, enabling it suitable for colorimetric/SERS dual-mode sensing. Scheme 1A described the high performance Au@AgPt NPs containing a plasmonic core (Au) wrapped by an irregular catalytic shell (Ag/Pt) that were effectively fabricated using a seed-mediated growth method combined with a galvanic replacement reaction. Specifically, CTAC-capped spherical Au NPs were used as cores for the growth of tiny Ag shell by AA reduction, with the change of color from wine-red to yellow. Then, the Ag atoms deposited on the surface of Au NPs acted as electron donors for the reduction and growth of Pt, at which the galvanic replacement reaction proceeded simultaneously between Ag shell and Pt precursor, eventually resulting in the fabrication of dark-brown Au@AgPt NPs (Figs. 1A and S1). TEM images demonstrated a morphological change from spherical Au NPs to rattle-like Au@AgPt NPs, containing an outer shell thickness of approximately 8 nm, interior nanogaps of approximately 10 nm, and an Au nanosphere of 20 nm within the core (Fig. S2). In comparison with previous method that utilized Au@Ag core-shell NPs as the sacrificial templates for Pt shell reduction [27], we fabricated Au@AgPt NPs in a co-deposition method with a larger hollow interior that might absorb more substrates for achieving high catalytic efficiency (Fig. S3).

Furthermore, EDX spectroscopy elemental mapping and line profiles analysis showed a uniform distribution of Ag/Pt atoms around the core area of Au atoms, which was indicative of the successful formation of Au@AgPt NPs (Figs. 1B, S4 and S5). The surface composition and the electronic interactions of elements

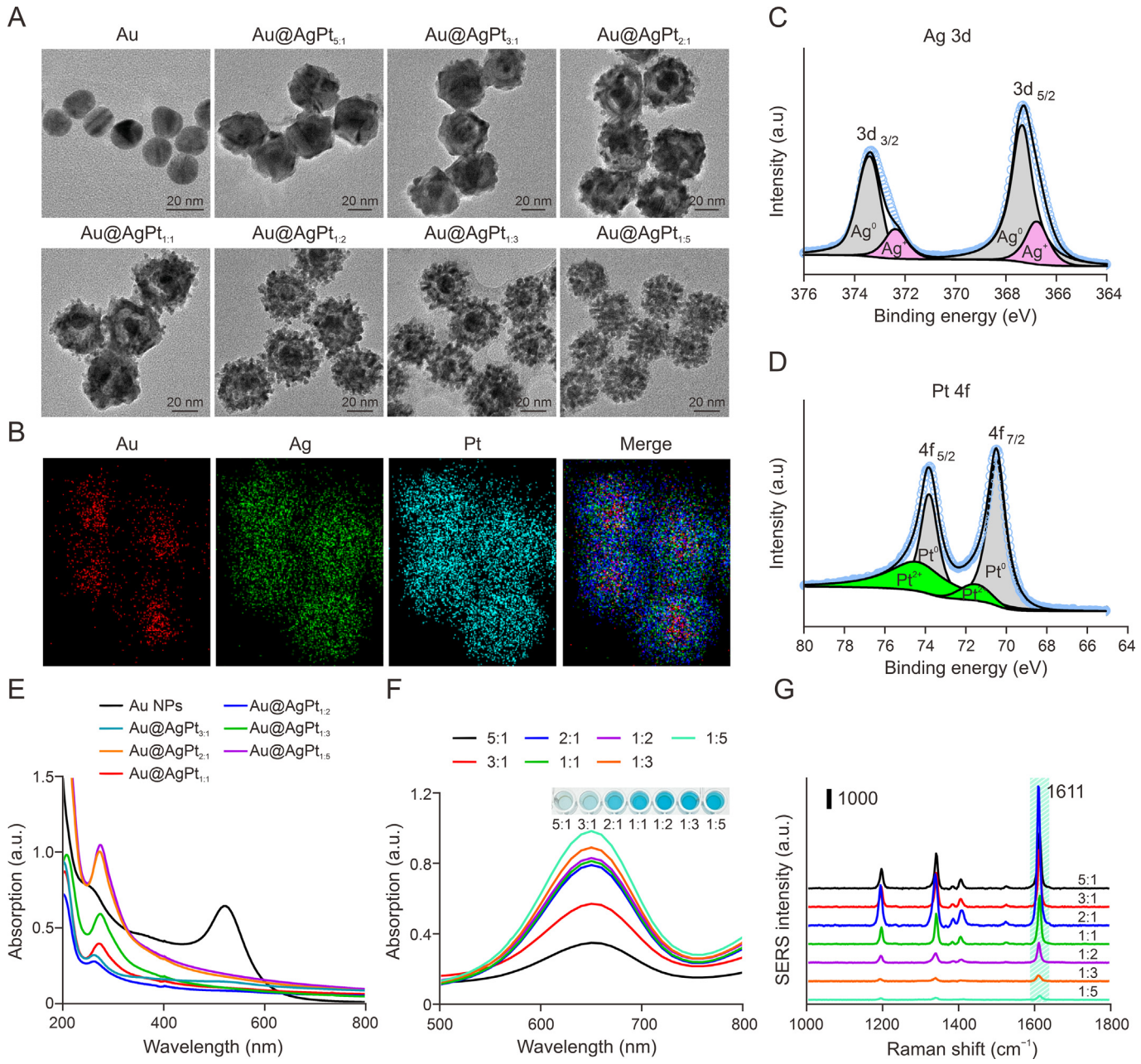

Fig. 1. Preparation and optimization of the Au@AgPt nanoparticles (NPs). (A) Representative transmission electron microscopy (TEM) images of Au NPs and Au@AgPt NPs fabricated with different Ag/Pt ratios (5:1, 3:1, 2:1, 1:1, 1:2, 1:3, and 1:5, *v/v*). (B) Transmission electron microscopy (TEM) elemental mapping images of Au@AgPt NPs. (C, D) High-resolution Ag 3d (C) and Pt 4f (D) X-ray photoelectron spectroscopy (XPS) spectra of Au@AgPt NPs. (E) Ultraviolet-visible (UV−vis) absorption spectra of Au@AgPt NPs fabricated with different Ag/Pt ratios. (F, G) UV−vis absorption spectra (F) and surface-enhanced Raman scattering (SERS) spectra (G) of 3,3',5,5'-tetramethylbenzidine (TMB) catalyzed by Au@AgPt NPs.

were also characterized using XPS, revealing the existence of Au, Ag, and Pt (Fig. S6). The spectrum of Ag showed double peaks attributed to Ag $3d_{3/2}$ and Ag $3d_{5/2}$ at binding energies of 373.3 and 367.3 eV, respectively; meanwhile, distinct peaks observed at 70.5 and 73.8 eV were attributed to Pt $4f_{7/2}$ and Pt $4f_{5/2}$ in the metallic state of Pt, respectively (Figs. 1C and D). Compared to the standard values of pure atomic Ag and Pt, the binding energies in Ag 3d shifted to higher values, whereas the Pt 4f peak underwent a concurrent negative binding energy shift, which ascertained migration of electrons from Ag sites to Pt sites occurs during the formation of the Ag/Pt alloy shell. The X-ray diffraction (XRD) pattern of Au@AgPt NPs further revealed the presence of the Au/Ag and Ag/Pt alloys (Fig. S7), which is in accordance with element composition of TEM mapping and XPS analysis.

Furthermore, the morphology and properties of Au@AgPt NPs were tuned by controlling the different dosage of $AgNO_3$ and H_2PtCl_6. The decrease ratio of Ag/Pt led to a constant drop in the LSPR peak (Fig. 1E), a positive shift in the surface charge (Fig. S8) and a change in the morphology of the NPs toward a rattle structure (Fig. 1A), whereas Au cores maintained their morphology well during the atomic transference of Ag and Pt. Undoubtedly, the more Ag shell it etched by the Pt precursor, the larger internal space and the thicker Ag/Pt layer it formed. This unique hollow structure endowed Au@AgPt NPs with the larger specific surface area, which

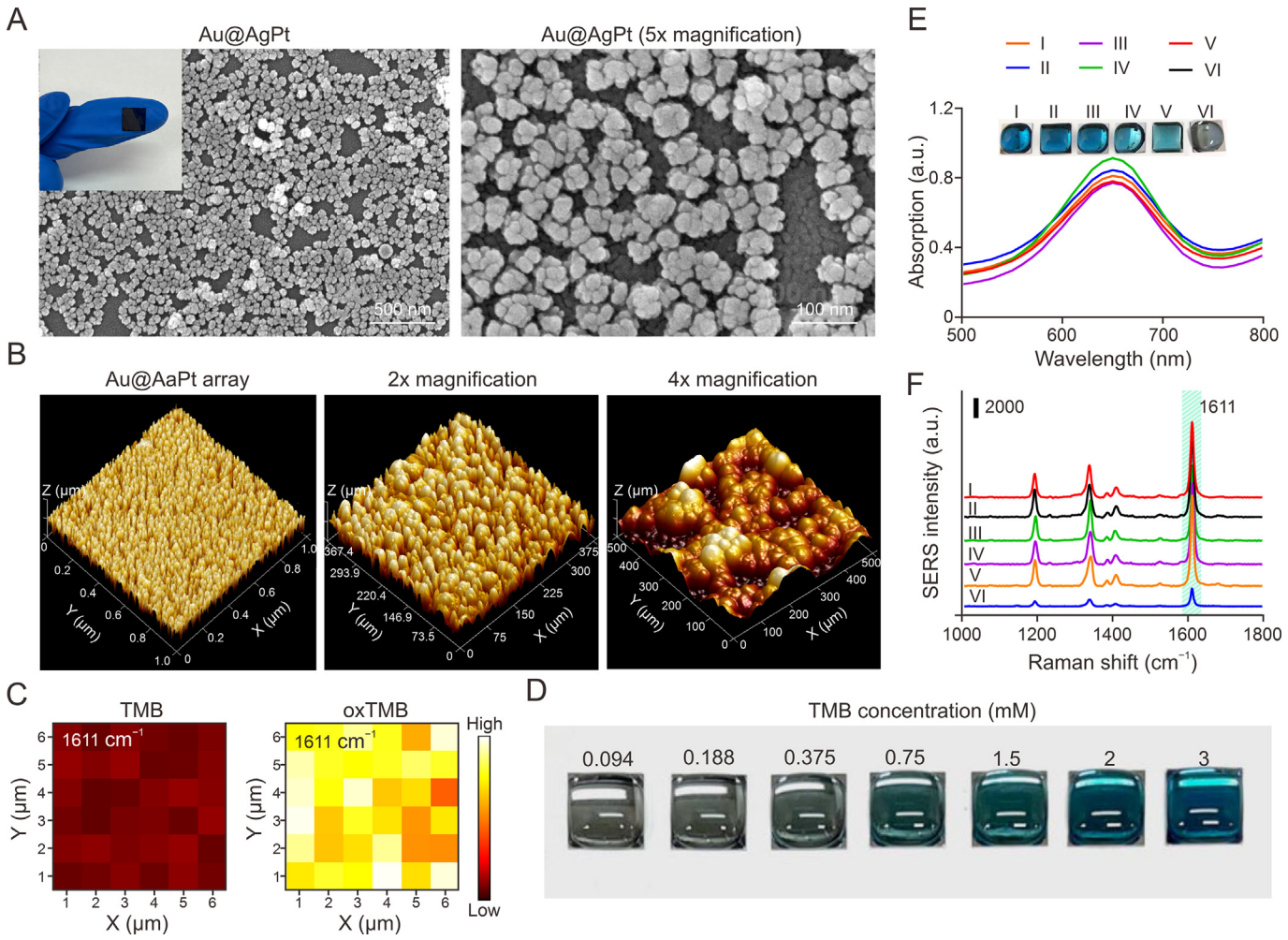

Fig. 2. Self-assembly of the Au@AgPt array. (A) Representative scanning electron microscopy (SEM) and enlarged image of Au@AgPt array. Inset: actual photograph of Au@AgPt substrate. (B) Atomic force microscopy (AFM) images of Au@AgPt array in different magnifications. (C) Surface-enhanced Raman scattering (SERS) mapping images (6 μm × 6 μm) were obtained at 1611 cm^{-1} before or after the catalytic reaction of 3,3',5,5'-tetramethylbenzidine (TMB). (D) Photographs taken after different concentrations of TMB reacting on Au@AgPt array. (E, F) Ultraviolet−visible (UV−vis) absorption (E) (inset: photograph of TMB solutions after different treated groups) and SERS (F) spectra of different treated groups. I: pure L-ascorbic acid 2-phosphotrisodium salt (AAP); II: alkaline phosphatase (ALP); III: ALP-DNA-magnetic beads (ALP-DNA-MBs); IV: ALP-DNA-MBs + micrococcal nuclease (MNase); V: ALP-DNA-MBs + AAP; and VI: ALP-DNA-MBs + AAP + MNase solutions, all of which reacted with TMB on Au@AgPt array. oxTMB: oxidized TMB.

is beneficial to the catalytic property and local electromagnetic field generation. However, overly dense Pt layer formed a fully encapsulated shell and might shield the plasmonic performance of Au@Ag, implying a decline in SERS enhancement. It has been demonstrated that nanozyme can catalyze the weak Raman signal of the parent diamine (TMB^0) to a radical cation (TMB^+), which mediates the production of charge transfer complex of the diamine with strong Raman signal. Therefore, we utilized TMB as a model catalytic substance and SERS-active molecules to explore a suitable etching ratio of Au@AgPt NPs that balances the catalytic-SERS signal activity. As displayed in Fig. S9, colorless TMB is oxidized by Au@AgPt NPs in the presence of H_2O_2, generating blue-colored oxTMB and characteristic absorption peaks at 652 nm. The absorption intensity went upward constantly with the increased content of Pt precursor and tended to equilibrium until the ratio of 2:1, at which Pt atoms had covered nearly all the surface of Au@AgPt NPs, causing TMB catalytic saturation (Fig. 1F). Moreover, the SERS-based biosensing of the Au@AgPt NPs was evaluated using SERS-active oxTMB upon a 633 nm extinction laser (1 mW) (Fig. S10). As recorded in Fig. 1G, the SERS characteristic peak of oxTMB at 1611 cm^{-1} provided evidence of the combination of C−H bending modes and ring stretching, whereas the bands at 1192 cm^{-1} and 1337 cm^{-1} were attributed to the CH_3 bending modes and inter-ring C−C stretching modes, respectively [38]. As the ratio of Ag/Pt continued to touch up to 2:1, SERS signal intensity reached a maximum, so the Ag/Pt ratio of 2:1 was selected as the optimized condition, at which the fabricated Au@AgPt NPs exhibited satisfactory SERS and catalytic signals. Under optimum conditions (pH = 4, 37 °C) for the catalytic reaction (Figs. S11 and S12), the steady-state kinetics calculated in Fig. S13 further proved the satisfactory affinity of Au@AgPt NPs for TMB, which is due to the larger specific surface area within the interior cavity that allows the substrate to fully interact with these catalytically active sites, thereby improving the overall catalytic efficiency.

3.2. Feasibility of Au@AgPt array for MNase activity detection

In this study, Au@AgPt NPs can not only observe the reaction in solution directly by the colorimetric assay, but also monitor the real catalytic process on the catalyst surface or interface via SERS assay. Unfortunately, the random NP aggregates in solution tend to produce SERS signals with poor reproducibility, inevitably leading to false positive or false negative results during detection. To overcome this disadvantage, constructing a well-organized nanostructured array

that allows analytes to quickly and tightly concentrate on the uniform "hot spots" seems to be an effective strategy. We induced colloidal Au@AgPt NPs to self-assemble into a thin monolayer film using an oil-water separation method and obtained highly reproducible SERS signals. Then, this film was transferred onto the silicon wafer to prepare a dense Au@AgPt array.

As revealed by SEM, a close-packed Au@AgPt array was prepared successfully with open and wide surface, where the abundant nanogaps between NPs could generate strong and uniform plasmonic coupling enhancement, affording great SERS activity (Fig. 2A). It was notable that different batches of Au@AgPt array also showed the satisfactory homogeneity, indicating the high repeatability of the signals acquired from each fabricated substrate (Fig. S14). However, the Au@AgPt NPs were dispersive with some cracks because of the ineluctable solvent volatilization during the transfer and drying process. Besides, the polarity of the organic solvent also played a vital role for self-assembly performance owing to the synergistic effect between interfacial energy and solvent polarity. In AFM imaging, the scanned area revealed a surface morphology characterized by rough bump shapes, with heights consistent with the results of SEM analysis, around 40 nm (Fig. 2B). The uniformly distributed NPs on the Si surface were essential for improving sensitivity in subsequent colorimetric/SERS analysis. Moreover, the SERS and catalytic performance was further characterized by the reaction of TMB, whose oxTMB as SERS-active molecules displayed the characteristic SERS peak at 1611 cm^{-1} (Figs. 2C and S15). It was obvious that an increasing amount of oxTMB caused blue color of the droplets to become deeper and the SERS signals increase (Figs. 2D and S16). In comparison to the conventional Au array, the Au@AgPt array exhibited stronger SERS and catalytic signals due to pronounced electromagnetic mechanism of Au/Ag NPs and mimetic enzyme activity of Pt shell (Fig. S17). Moreover, fast evaluation of MNase at room temperature can be achieved by this colorimetric/SERS-based array, which will address the high-throughput detecting of analytes.

To further estimate repeatability of this prepared Au@AgPt array, we randomly tested 12 spots on the array and compared the signal change of the correlative SERS peak after reaction with TMB substrate. Results revealed that the relative standard deviation (RSD) of SERS signals at different locations was only 5.42%, further manifesting the great uniformity of this Au@AgPt array (Fig. S18). Besides, long-term stability is also a crucial index that should be considered for the Au@AgPt array. To further evaluate their catalytic stability, we stored the Au@AgPt substrate in the dark at 4 °C for varying durations, followed by a catalysis reaction with TMB for analysis. Fig. S19 showed that even after 10 days of storage, the SERS intensity and catalytic activity of the Au@AgPt array remained high.

Given the aforementioned outstanding properties, the feasibility of Au@AgPt array for following MNase detection was further determined by colorimetric/SERS dual-model sensing. As illustrated in Scheme 1C, the free ALP cleaved by MNase can catalyze the conversion of AAP into AA that mediated the afterward reduction of oxTMB, accompanying with the conversion of solution from blue to colorless and the distinct diminishment of SERS intensity. The change in absorbance and SERS signals of the TMB reaction were assessed via several controlled experiments. After incubation on the Au@AgPt array, the blue oxTMB cannot be reversed in the AAP, ALP, or ALP-DNA-MB alone, all of which exhibited significant absorption spectra of oxTMB (Fig. 2E). Also, there was the negligible change of color or absorption signal in other control groups including ALP-DNA-MB + MNase and ALP-DNA-MB + AAP. Only when MNase cleaved DNA strand on MB did the ALP release in the solutions to react with AAP for the production of AA, which can mediate the reduction of oxTMB, causing the blue color to fade and a decline in absorbance. The colorimetric results were further supported by the SERS assay (Fig. 2F), in which a distinctive SERS signal of oxTMB appeared without the addition of MNase, while its Raman peak diminished rapidly once MNase-initiated cascade generation of AA. Hence, all these results strongly confirmed the validity of Au@AgPt array for colorimetric/SERS detecting the target MNase.

3.3. Sensitivity of Au@AgPt array for MNase detection

We further investigated the sensitivity of the proposed Au@AgPt array based on its excellent response to the MNase. Initially, the obvious colorimetric/SERS signal of oxTMB was obtained on the Au@AgPt array. As the MNase concentration increased, the cascade reaction led to the formation of more AA, causing the colorimetric/SERS signal of oxTMB to fade away (Fig. 3A). As depicted in Fig. 3B, the colorimetric intensity of oxTMB at 652 nm gradually decreased with the increasing concentration of MNase from 25 to 800 U/L. The regression equation was $Y = -0.0014X + 1.205$, (Y represented the absorption intensity at 652 nm; X represented the MNase concentration), demonstrating a good linear correlation. The squares of correlation coefficients (R^2) was 0.991, and the calculated LOD toward MNase was 8.6 U/L, determined by three times the SD of the background.

For SERS analysis, MNase was detected by recording the SERS intensity of oxTMB. Similar to the colorimetric results, SERS intensities also decreased with increasing MNase concentration (Fig. 3C), while showing nonlinear as the concentration increased to over 400 U/L (Fig. 3D). A good linear plot was obtained in the concentration range of 5–400 U/L (Fig. 3E), and the SERS mapping profile presented a uniform signal output across the selected region (64 pixel points in a 8 μm × 8 μm area on the array), further illustrating the weak SERS signal of oxTMB with the increasing concentration of the target MNase (Fig. 3F). The linear relationship equation was $Y = -18.76X + 9748.7$ (Y represented the SERS intensity at 1611 cm^{-1}; X represented the MNase concentration) with a LOD of 2.3 U/L ($R^2 = 0.985$), which is much lower than that of the colorimetric model, elucidating the high sensitivity of SERS sensing toward MNase detection. However, in comparison with SERS mode, colorimetric visualization mode is more convenient, direct and has a wider detection range for MNase detection. Therefore, the integration of dual-mode detection displayed the inherent characteristics of each mode, and also gave more choices and double insurance on the same analysis, thereby enhancing the accuracy and reliability of results. Although the LOD is comparable with the reported optical sensors, our SERS/colorimetric method has the advantage of a wider linear range, demonstrating great potential to meet the requirements of different cases (Table S1) [39–42].

The specificity of MNase-based strategy was validated by incubating other interference nucleases (all at 800 U/L), such as Exo I, Exo III, and DNase I, on the Au@AgPt array. A sample without nucleases was the negative control (the blank group). As given in Figs. 3G and H, an evident color change appeared only in the presence of the target MNase, whereas the signals from other nucleases were almost similar as that of the blank group, which was further confirmed by the SERS results (Fig. S20). It is reasonable because MNase is an unusually thermostable enzyme so that it stays alive and active even under high temperature conditions, while other interfering enzymes distributed in the system are denatured during the heat treatment, thus vastly improving the anti-interference ability of MNase detection. Besides, the magnetic-assisted separation and enrichment is also benefit to achieve the more sensitive and selective detection. To further unveil this strategy for specifically responding toward MNase, inhibition experiments were performed by pretreating MNase with a common inhibitor,

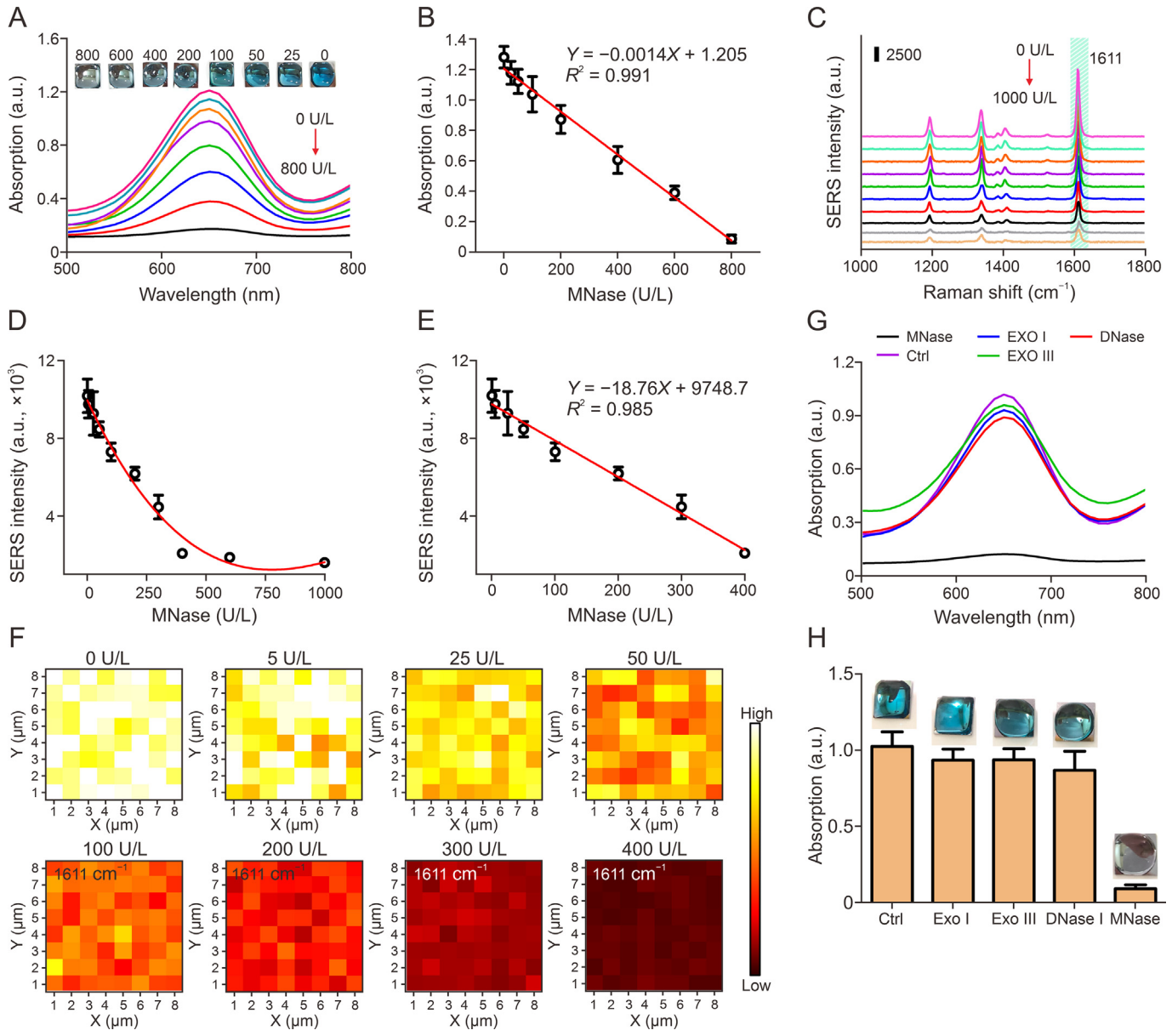

Fig. 3. Sensitivity and specificity of Au@AgPt array for micrococcal nuclease (MNase) detection. (A) Ultraviolet−visible (UV−vis) absorption of 3,3',5,5'-tetramethylbenzidine (TMB) after cascade-reaction induced by various concentrations of micrococcal nuclease (MNase) on Au@AgPt array (inset: photograph of TMB solutions on Au@AgPt array treated according to Fig. 3A). (B) Linear relationships between MNase concentration and absorption intensity at 652 nm (25−800 U/L). (C) Surface-enhanced Raman scattering (SERS) signal of oxidized TMB (oxTMB) after cascade-reaction induced by different MNase concentrations on Au@AgPt array. (D) Linear relationships between MNase concentration and SERS intensity at 1611 cm^{-1} (5−1000 U/L). (E) Calibration curve of SERS intensity versus the concentration of MNase (5−400 U/L). (F) SERS mapping images (8 μm × 8 μm) obtained at 1611 cm^{-1} with the increasing concentration of MNase (5−400 U/L). (G) Specificity of MNase against other interference nucleases (800 U/L; n = 3/group). (H) UV−vis absorption intensity at 652 nm according to Fig. 3G (inset: photograph of oxTMB solutions on Au@AgPt array treated according to Fig. 3G). Data are presented as mean ± standard deviation (SD). Exo: exonuclease; DNase: deoxyribonuclease.

ethylene diamine tetraacetic acid (EDTA), to lower its catalytic ability. As expected, the colorimetric/SERS signal were substantially recovered as the inhibitor concentration increase (Fig. S21), further proving that MNase activity restrained by EDTA fails to trigger ALP release for subsequent oxTMB reduction. Therefore, the inhibition assay further verified the specificity of this strategy toward MNase, which foreboded the detection of *S. aureus* using MNase activity available.

3.4. Sensitive colorimetric/SERS sensing for S. aureus

S. aureus assay was conducted by using MNase enzyme as a unique indicator due to the strong correlation between heat-stable MNase and *S. aureus* count. Although this strategy showed great feasibility in the detection of MNase, the component of these artificial MNase samples is pure and unitary, and the MNase released from *S. aureus* is often susceptible to complicated environment; therefore, whether their activity can be tested remains to be evaluated. Here, the boiling *S. aureus* solution was separated through centrifugation, mixed with ALP-DNA-MB to induce the release of ALP, and incubated with AAP on the Au@AgPt array for colorimetric/SERS sensing, as a similar detection procedure above. As shown in Fig. S22, an apparent absorption and SERS spectra decrease of oxTMB was observed once MNase secreted from *S. aureus* underwent sequential cascade reaction for oxTMB reduction. Specifically, the colorimetric intensity of the oxTMB gradually

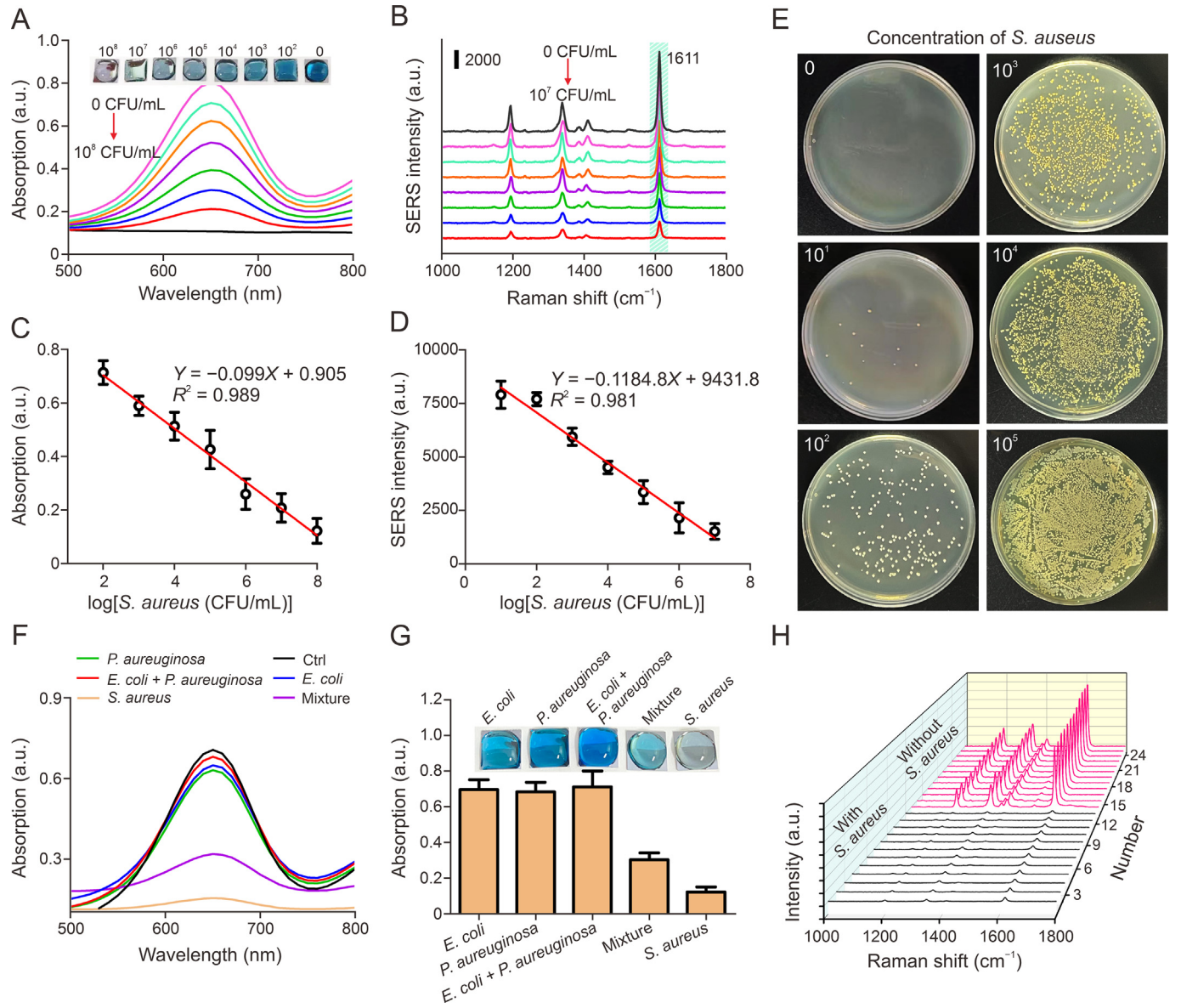

Fig. 4. Sensitive colorimetric/surface-enhanced Raman scattering (SERS) sensing for *Staphylococcus aureus*. (A, B) Colorimetric (A) and SERS response (B) of the cascade triggering strategy induced by various concentrations of *S. aureus* on Au@AgPt array. (C, D) Plot of ultraviolet–visible (UV–vis) (C) and SERS peak (D) intensities versus the logarithmic concentration of *S. aureus* spiked in phosphate-buffered saline (PBS). (E) The results of colony counting verified the reliability of colorimetric/SERS sensing. (F) Specificity analysis of *S. aureus*. Samples contained either target *S. aureus* and/or other interfering bacteria (10 times more than target *S. aureus*). (G) Signal intensities of UV–vis for Fig. 4F (inset: photograph of oxidized 3,3',5,5'-tetramethylbenzidine (oxTMB) reaction induced by different bacteria). Data are presented as mean ± standard deviation (SD). (H) 12 randomly selected SERS spectra acquired before or after *S. aureus*-mediated cascade process. *E. coli*: *Escherichia coli*; *P. aeruginosa*: *Pseudomonas aeruginosa*.

descended as the enhancing concentration of *S. aureus* from 10^2 CFU/mL to 10^8 CFU/mL (Fig. 4A). The visual readout demonstrated very good linear relationships as seen in Fig. 4C ($R^2 = 0.989$), where the linear equation was $Y = -0.099X + 0.905$ (Y represented the absorption intensity at 652 nm; X represented the logarithmic concentration of *S. aureus*) with a LOD of 38 CFU/mL. Furthermore, SERS intensity of oxTMB also decreased steadily as the concentration of *S. aureus* enhanced from 10 CFU/mL to 10^7 CFU/mL (Fig. 4B). The linear equations were obtained ($R^2 = 0.981$), resulting in $Y = -1184.8X + 9431.8$ (Y represented the SERS intensity at 1611 cm^{-1}; X represented the logarithmic concentration of *S. aureus*) with the LOD of 6 CFU/mL (Fig. 4D). These quantitative results determined by colorimetric and SERS sensing agreed well with those of plate count method (Fig. 4E), which fully substantiated the high accuracy and reliability of our strategy.

To investigate the specificity of this method for *S. aureus*, two interfering bacteria containing *E. coli* and *P. aeruginosa* were examined on the Au@AgPt array under the same experimental conditions. Unlike the rapid signal attenuation of the target *S. aureus*, other bacteria had less effect on the oxTMB signal (Figs. 4F and G). Accordingly, this colorimetric/SERS assay showed a selective response toward *S. aureus*. To further confirm the selectivity of the as-proposed assay, all interfering bacteria were mixed with *S. aureus*. Predictably, the signal intensity of the mixed group was basically the same as that of simple *S. aureus* alone. Thus, the high selectivity should be attributed to the ingenious design of the MNase-triggered cascade response and the reliable colorimetric/SERS dual-mode sensing mediated by Au@AgPt array. To further assess the reproducibility of this method, 12 of SERS spectra from the different areas were collected and the colorimetric/SERS signal variation was

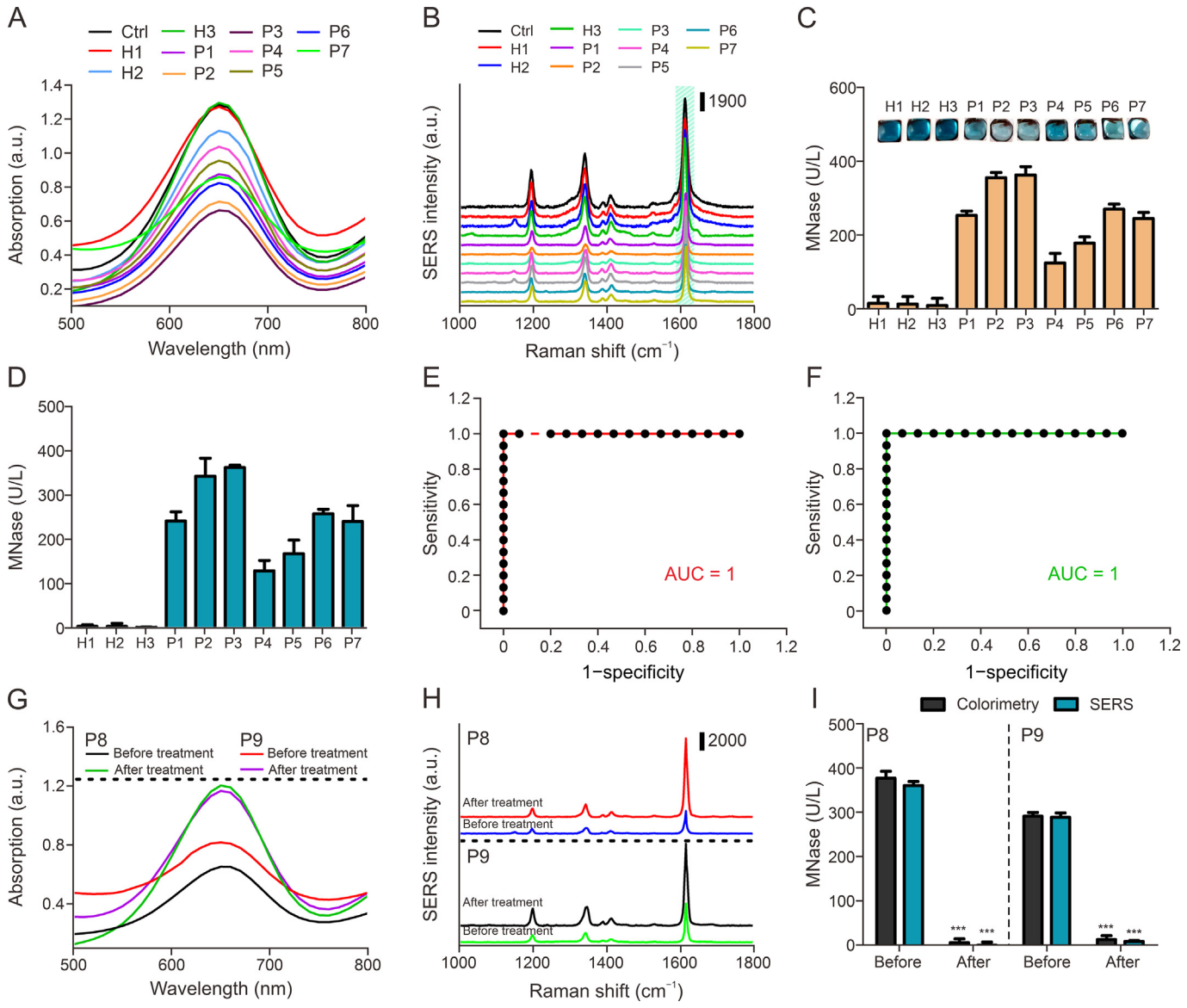

Fig. 5. The applicability of this strategy in clinical samples. (A, B) Absorption (A) and surface-enhanced Raman scattering (SERS) spectra (B) of oxidized 3,3',5,5'-tetramethylbenzidine (oxTMB) in different clinical samples after cascade triggering strategy. (C, D) The expression levels of micrococcal nuclease (MNase) in healthy humans ($n = 3$, H1 to H3) and patients with sepsis ($n = 7$, P1 to H7) recorded by colorimetric (C) and SERS assay (D). (E, F) Receiver operating characteristic (ROC) curves for patients with sepsis based on MNase in colorimetric (E) and SERS (F) modes. (G, H) Absorption (G) and SERS (H) spectra of oxTMB in patients with sepsis before or after treatment ($n = 2$, P8 and P9). (I) MNase expression levels of patients with sepsis before or after treatment recorded by colorimetric and SERS assay. $^{***}P < 0.001$. Data are presented as mean ± standard deviation (SD). H: healthy candidates; P: patient samples; AUC: area under the receiver operating characteristic curve.

observed. After *S. aureus*-mediated cascade process, all the SERS intensity of oxTMB dropped rapidly on the nanoarray (Fig. 4H). The favorable repeatability is ascribed to the symmetric arrangement of "hot spots" on the Si interface, thus providing the promising reliability for the further *S. aureus* detection in real clinical samples.

3.5. Application analysis of serum samples

As a promising strategy for *S. aureus* detection, its feasibility and application in real human serum sample need to be verified. To avoid the severe matrix effects from the serum, we spiked different amounts of the target pathogen (*S. aureus*) into 1% real samples and obtained recoveries above 93.7% with RSD levels all below 10% (Table S2). This is because the high selectivity of "on-off" cascade triggering strategy of MNase on the Au@AgPt interface made the satisfactory diagnosis performance even under the interference of various serum proteins.

To further assess this cascade triggering strategy for clinical applications, we challenged our Au@AgPt array with 10 clinical serum samples from healthy participants (H1 to H3) and patients with sepsis (P1 to P7) that were identified by standard plate counting from the clinical laboratory of the hospital. The MNase levels were converted according to the standard curves of colorimetric/SERS signals. Predictably, MNase levels were abnormally elevated in patients with sepsis compared with healthy volunteers, as evidenced by data recorded from colorimetric (Figs. 5A and B) and SERS analysis (Figs. 5C and D). Next, the receiver operating characteristic (ROC) curves were depicted in Figs. 5E and F, where the area under curve (AUC) was calculated to be 1 for both colorimetric and SERS model by a ROC curve analysis, further verifying the distinguished

performance of this diagnostic method. Although the specific threshold range did not set up in our work due to insufficiency of the collected patient samples, there is a considerable difference in MNase content between healthy participants and patients with sepsis; thus, this MNase-mediated strategy successfully distinguishes patients with sepsis from healthy participants and has the potential for early-stage patient screening. Accurately determining the therapy response from patients considerably affects the instruction of clinical medication. Notably, the patients with sepsis (P8 and P9) showed a low level of MNase level after certain days of antibiotic therapy (approximately two weeks), further indicating the availability of this sensing strategy for monitoring disease progression and assessing treatment response (Figs. 5G–I). This information is helpful for patients to provide personalized treatment and regimen, which can substantially improve the cure rates of patients.

In clinical samples, myriad impurities, including other microorganisms, proteins, and organic and inorganic substances, can interact with sensing probe due to the nonspecific absorption [43,44], inevitably leading to false-positive/negative results during measurement. Fortunately, the target MNase detected in this study is thermostable nuclease, which enabled them to avoid interference from other impurities in the complex biological fluids that are unstable or even inactive after short heating procedure. Of particular significance is the subsequent magnetic separation mediated by the magnetic bead, which further boosted the anti-interference ability of the assay. Therefore, our proposed strategy conferred the ability to quickly measure clinical real samples with great sensitivity and accuracy, which would be a promising approach for diagnosing *S. aureus* infections in clinical settings.

4. Conclusion

In summary, we herein constructed an ordered monolayer Au@AgPt array that integrated incomparable peroxidase-mimicking and SERS properties for colorimetric/SERS sensing MNase, a unique indicator for *S. aureus*. Compared with the traditional microbial culture method, this strategy substantially shortened sample-to-answer time with superior selectivity and sensitivity, owing to the ingenious design of MNase-mediated cascade response, high interferent resistance of magnetic separation technology, and high and stable signal output from the nanoarray. Based on these favorable properties, this MNase-mediated strategy can be effectively applied in serum assays of patients with sepsis to distinguish between positive and negative samples and potentially guide the prognosis of patients with sepsis. More importantly, the visualization analysis made the results more intuitive and reduced the reliance on large-scale instruments, which can meet the requirement of POC testing in clinic. However, at the current stage, the sample still requires serum dilution, centrifugation, and multiple pipetting steps before the results can be read on the Au@AgPt array. Future research objectives include further minimizing response time, overcoming technical barriers, and lowering costs by combining this detection method with portable lasers, spectrometers and chips for early warning of *S. aureus* infections.

CRediT authorship contribution statement

Xueqin Huang: Methodology, Funding acquisition, Formal analysis, Data curation, Writing – original draft. **Yingqi Yang:** Formal analysis, Data curation, Writing – original draft. **Hanlin Zhou:** Data curation. **Liping Hu:** Data curation. **Annan Yang:** Data curation. **Biying Zheng:** Data curation. **Jiang Pi:** Data curation. **Jun Xu:** Data curation. **Pinghua Sun:** Supervision. **Huai-Hong Cai:** Data curation. **Xujing Liang:** Data curation. **Bin Pan:** Data curation. **Junxia Zheng:** Resources, Funding acquisition, Conceptualization. **Haibo Zhou:** Supervision, Resources, Project administration, Investigation, Conceptualization, Writing – review & editing.

Declaration of competing interest

The authors declare that there are no conflicts of interest.

Acknowledgments

This work is financially supported by the National Natural Science Foundation of China (Grant Nos.: 82373833, 22177039, and 82304438), the National Key Research and Development Program of China (Grant No.: 2021YFC2300400), and Guangdong Basic and Applied Basic Research Foundation, China (Grant Nos.: 2024A1515012204, 2022A1515010300, and 2022A1515110618). We gratefully acknowledges the support of K. C. Wong Education Foundation, China. We are very grateful for the testing services provided by the Analysis and Test Center of Jinan University, China. The computational analysis in this research was supported by the High Performance Public Computing Service Platform of Jinan University, China.

Appendix A. Supplementary data

Supplementary data to this article can be found online at https://doi.org/10.1016/j.jpha.2024.101085.

References

1 T.L. Burke, M.E. Rupp, P.D. Fey, *Staphylococcus epidermidis*, Trends Microbiol 31 (2023) 763–764.
2 J.M. Kwiecinski, A.R. Horswill, *Staphylococcus aureus* bloodstream infections: Pathogenesis and regulatory mechanisms, Curr. Opin. Microbiol. 53 (2020) 51–60.
[3] S.S. Samani, A. Khojastehnezhad, M. Ramezani, et al., Ultrasensitive detection of micrococcal nuclease activity and *Staphylococcus aureus* contamination using optical biosensor technology-a review, Talanta 226 (2021), 122168.
[4] J. Allan, R.M. Fraser, T. Owen-Hughes, et al., Micrococcal nuclease does not substantially bias nucleosome mapping, J. Mol. Biol. 417 (2012) 152–164.
[5] Y. He, L. Xiong, X. Xing, et al., An ultra-high sensitive platform for fluorescence detection of micrococcal nuclease based on graphene oxide, Biosens. Bioelectron. 42 (2013) 467–473.
[6] S.P. Yazdankhah, L. Sølverød, S. Simonsen, et al., Development and evaluation of an immunomagnetic separation-ELISA for the detection of *Staphylococcus aureus* thermostable nuclease in composite milk, Vet. Microbiol. 67 (1999) 113–125.
[7] E.A. Ottesen, J.W. Hong, S.R. Quake, et al., Microfluidic digital PCR enables multigene analysis of individual environmental bacteria, Science 314 (2006) 1464–1467.
[8] D. Kang, M.M. Ali, K. Zhang, et al., Rapid detection of single bacteria in unprocessed blood using Integrated Comprehensive Droplet Digital Detection, Nat. Commun. 5 (2014), 5427.
[9] J. Zhou, R. Fu, F. Tian, et al., Dual enzyme-induced Au-Ag alloy nanorods as colorful chromogenic substrates for sensitive detection of *Staphylococcus aureus*, ACS Appl. Bio Mater. 3 (2020) 6103–6109.
[10] Y. Chen, L. Wang, W. Jiang, Micrococcal nuclease detection based on peptide-bridged energy transfer between quantum dots and dye-labeled DNA, Talanta 97 (2012) 533–538.
[11] X. Huang, Z. Zhang, L. Chen, et al., Multifunctional Au nano-bridged nanogap probes as ICP-MS/SERS dual-signal tags and signal amplifiers for bacteria discriminating, quantitative detecting and photothermal bactericidal activity, Biosens. Bioelectron. 212 (2022), 114414.
[12] X. Huang, B. Sheng, H. Tian, et al., Real-time SERS monitoring anticancer drug release along with SERS/MR imaging for pH-sensitive chemo-phototherapy, Acta Pharm. Sin. B 13 (2023) 1303–1317.
[13] X. Huang, Q. Chen, Y. Ma, et al., Chiral Au nanostars for SERS sensing of enantiomers discrimination, multibacteria recognition and photothermal antibacterial application, Chem. Eng. J. 479 (2024), 147528.
[14] J.Y. Kim, D. Han, G.M. Crouch, et al., Capture of single silver nanoparticles in nanopore arrays detected by simultaneous amperometry and surface-enhanced Raman scattering, Anal. Chem. 91 (2019) 4568–4576.
[15] S. Xiang, C. Ge, S. Li, et al., *In situ* detection of endotoxin in bacteriostatic process by SERS chip integrated array microchambers within bioscaffold nanostructures and SERS tags, ACS Appl. Mater. Interfaces 12 (2020) 28985–28992.

[16] L. Zhang, R. Hao, D. Zhang, et al., Shape-controlled hierarchical flowerlike Au nanostructure microarrays by electrochemical growth for surface-enhanced Raman spectroscopy application, Anal. Chem. 92 (2020) 9838–9846.
[17] X. Zhou, H. Huang, Y. Yang, et al., Dendritic alloy shell Au@AgPt yolk sensor with excellent dual SERS enhancement and catalytic performance for *in situ* SERS monitoring reaction, Sensor. Actuator. B Chem. 394 (2023), 134385.
[18] J. Li, W. Liu, X. Wu, et al., Mechanism of pH-switchable peroxidase and catalase-like activities of gold, silver, platinum and palladium, Biomaterials 48 (2015) 37–44.
[19] Y. Lin, J. Ren, X. Qu, Nano-gold as artificial enzymes: Hidden talents, Adv. Mater. Deerfield Beach Fla 26 (2014) 4200–4217.
[20] J. Liu, L. Meng, Z. Fei, et al., On the origin of the synergy between the Pt nanoparticles and MnO_2 nanosheets in Wonton-like 3D nanozyme oxidase mimics, Biosens. Bioelectron. 121 (2018) 159–165.
[21] C. Wang, Y. Gao, S. Hu, et al., MnO_2 coated Au nanoparticles advance SERS detection of cellular glutathione, Biosens. Bioelectron. 215 (2022), 114388.
[22] Y. Li, P. Li, Y. Chen, et al., Interfacial deposition of Ag nanozyme on metal-polyphenol nanosphere for SERS detection of cellular glutathione, Biosens. Bioelectron. 228 (2023), 115200.
[23] L. Wang, Y. Chen, Y. Ji, et al., Cheap and portable paper chip with terrific oxidase-like activity and SERS enhancement performance for SERS-colorimetric bimodal detection of intracellular glutathione, Biosens. Bioelectron. 244 (2024), 115817.
[24] Y. Huang, Y. Gu, X. Liu, et al., Reusable ring-like Fe_3O_4/Au nanozymes with enhanced peroxidase-like activities for colorimetric-SERS dual-mode sensing of biomolecules in human blood, Biosens. Bioelectron. 209 (2022), 114253.
[25] Y. Wang, K. Jiang, J. Zhu, et al., A FRET-based carbon dot-MnO_2 nanosheet architecture for glutathione sensing in human whole blood samples, Chem. Commun. Camb. Engl. 51 (2015) 12748–12751.
[26] T. Bai, L. Wang, M. Wang, et al., Strategic synthesis of trimetallic Au@Ag-Pt nanorattles for ultrasensitive colorimetric detection in lateral flow immunoassay, Biosens. Bioelectron. 208 (2022), 114218.
[27] X. Huang, L. Chen, T. Sha, et al., *In situ* tyrosinase monitoring by wearable microneedle patch toward clinical melanoma screening, ACS Nano 17 (2023) 20073–20086.
[28] X. Huang, H. Tian, L. Huang, et al., Well-ordered Au nanoarray for sensitive and reproducible detection of hepatocellular carcinoma-associated miRNA *via* CHA-assisted SERS/fluorescence dual-mode sensing, Anal. Chem. 95 (2023) 5955–5966.
[29] T. Kang, J. Zhu, X. Luo, et al., Controlled self-assembly of a close-packed gold octahedra array for SERS sensing exosomal microRNAs, Anal. Chem. 93 (2021) 2519–2526.
[30] S. Shanmukh, L. Jones, J. Driskell, et al., Rapid and sensitive detection of respiratory virus molecular signatures using a silver nanorod array SERS substrate, Nano Lett. 6 (2006) 2630–2636.
[31] D. Dong, L.W. Yap, D.M. Smilgies, et al., Two-dimensional gold trisoctahedron nanoparticle superlattice sheets: Self-assembly, characterization and immunosensing applications, Nanoscale 10 (2018) 5065–5071.
[32] S. Weng, D. Lin, S. Lai, et al., Highly sensitive and reliable detection of microRNA for clinically disease surveillance using SERS biosensor integrated with catalytic hairpin assembly amplification technology, Biosens. Bioelectron. 208 (2022), 114236.
[33] B. Feng, X. Pan, T. Liu, et al., A broadband photoelectronic detector in a silicon nanopillar array with high detectivity enhanced by a monolayer graphene, Nano Lett. 21 (2021) 5655–5662.
[34] J. Wang, J. Wu, Y. Zhang, et al., Colorimetric and SERS dual-mode sensing of mercury (II) based on controllable etching of Au@Ag core/shell nanoparticles, Sensor. Actuator. B Chem. 330 (2021), 129364.
[35] J. Wu, X. Zhou, P. Li, et al., Ultrasensitive and simultaneous SERS detection of multiplex microRNA using fractal gold nanotags for early diagnosis and prognosis of hepatocellular carcinoma, Anal. Chem. 93 (2021) 8799–8809.
[36] L. Li, W.S. Chin, Rapid and sensitive SERS detection of melamine in milk using Ag nanocube array substrate coupled with multivariate analysis, Food Chem. 357 (2021), 129717.
[37] L. Chen, X. Huang, X. Zeng, et al., Signal-on bimodal sensing glucose based on enzyme product-etching MnO_2 nanosheets for detachment of MoS_2 quantum dots, Chin. Chem. Lett. 32 (2021) 1967–1971.
[38] X. Ma, S. Wen, X. Xue, et al., Controllable synthesis of SERS-active magnetic metal-organic framework-based nanocatalysts and their application in photoinduced enhanced catalytic oxidation, ACS Appl. Mater. Interfaces 10 (2018) 25726–25736.
[39] S. Huang, Q. Xiao, Z. He, et al., A high sensitive and specific QDs FRET bioprobe for MNase, Chem. Commun. Camb. Engl. (2008) 5990–5992.
[40] T. Qiu, D. Zhao, G. Zhou, et al., A positively charged QDs-based FRET probe for micrococcal nuclease detection, Anales 135 (2010) 2394–2399.
[41] Y. Peng, J. Jiang, R. Yu, Label-free and sensitive detection of micrococcal nuclease activity using DNA-scaffolded silver nanoclusters as a fluorescence indicator, Anal. Methods 6 (2014) 4090–4094.
[42] D. Li, J. Qin, G. Yan, A phosphorescent sensor for detection of Micrococcal nuclease base on phosphorescent resonance energy transfer between quantum dots and DNA-ROX, Sensor. Actuator. B Chem. 255 (2018) 529–535.
[43] X. Huang, H. Cai, H. Zhou, et al., Cobalt oxide nanoparticle-synergized protein degradation and phototherapy for enhanced anticancer therapeutics, Acta Biomater. 121 (2021) 605–620.
[44] X. Huang, L. Chen, Y. Lin, et al., Tumor targeting and penetrating biomimetic mesoporous polydopamine nanoparticles facilitate photothermal killing and autophagy blocking for synergistic tumor ablation, Acta Biomater. 136 (2021) 456–472.